Microbranching in mode-I fracture in a randomly perturbed lattice

Shay I. Heizler,[1,2] David A. Kessler,[1,*] and Yonatan S. Elbaz[2]

[1]*Department of Physics, Bar-Ilan University, Ramat-Gan 52900, Israel*

[2]*Department of Physics, Nuclear Research Center-Negev, P.O. Box 9001, Beer Sheva 84190, Israel*

We study mode-I fracture in lattices using atomistic simulations with randomly distributed bond lengths. By using a small parameter that measures the variation of the bond length between the atoms in perfect lattices and using a three-body force law, simulations reproduce the qualitative behavior of the beyond-steady-state cracks in the high-velocity regime, including reasonable microbranching. In particular, the effect of the lattice structure on the crack appears minimal, even though in terms of the physical properties such as the structure factor $g(r)$ and the radial or angular distributions, these lattices share the physical properties of perfect lattices rather than those of an amorphous material (e.g., the continuous random network model). A clear transition can be seen between steady-state cracks, where a single crack propagates in the midline of the sample, and the regime of unstable cracks, where microbranches start to appear near the main crack, in line with previous experimental results. This is seen in both a honeycomb lattice and a fully hexagonal lattice. This model reproduces the main physical features of propagating cracks in brittle materials, including the total length of microbranches as a function of driving displacement and the increasing amplitude of oscillations of the electrical resistance. In addition, preliminary indications of power-law behavior of the microbranch shapes can be seen, potentially reproducing one of the most intriguing experimental results of brittle fracture. There was found to exist a critical degree of disorder, i.e., a sharp threshold between the cleaving behavior characterizing perfect lattices and the microbranching behavior that characterizes amorphous materials.

I. INTRODUCTION AND BRIEF REVIEW

Extensive experimental efforts devoted to the study of mode-I (tensile) fracture in amorphous materials have been undertaken in the past two decades [1–12] (for a review, see [13]). In the high-crack-velocity regime, the simple picture of a rapid steady-state crack generated via a given driving displacement and exhibiting a given crack velocity (of the order of the Rayleigh surface wave speed) breaks down and small microbranches start to appear next to the main crack [5–10,12]. Upon further increase of the loading, the microscopic branches transform to large macrobranches.

The experimental observation of this instability has been the subject of extensive theoretical effort as well. There have been several attempts within the framework of continuum models, based on the linear elasticity fracture mechanics (LEFM) theory [14]. Yoffe predicted that steady-state cracks will become unstable at a specific crack velocity $v_{cr} \approx 0.73c_R$, based on maximal stress considerations [15]. Another *ad hoc* attempt based on energy considerations predicted a critical velocity of $v_{cr} \approx 0.5c_R$ [16]. However, the mode-I experiments have shown material-dependent features, refuting those LEFM predictions. For example, the terminal crack speed observed in a number of brittle materials varies in the range $0.3 \leqslant v/c_R \leqslant 0.9$ (see Table 3 in [13]). In addition, there seems to be no basis for a universal critical velocity for macroscopic crack branching with reported values including: $0.18c_R$–$0.3c_R$ for glass, $0.78c_R$ for poly(methyl methacrylate) (PMMA), and $0.34c_R$–$0.53c_R$ for Homalite-100 [13]. Concerning the critical velocity for the microbranching instability, Adda-Bedia has argued for a material-dependent critical velocity, varying in

the range $0.3 \leqslant v/c_R \leqslant 0.42$ (see Fig. 8 in [17]). In addition, recent works in gels have shown an acceleration dependence of the critical velocity, up to $v \leqslant 0.75c_R$ [18]. Earlier hints for this phenomenon can be found also in [19,20]. Several LEFM-based works predict a microbranching instability at a material-dependent critical velocity [17]; however, the specific parameter that determines the specific critical velocity $\Gamma(v_{cr})$ is an input parameter to the theory.

Additional efforts have been made to explore the microbranching phenomenon based on LEFM [21,22]. However, as these works themselves argue, although they recover some features of the microbranching instability, some main predictions are unphysical. One notable example is the immediate interruption of energy flow to a newly formed microbranch, leading to its sudden arrest. These results raise the possibility that the microbranching phenomenon is a three-dimensional (3D) phenomenon, while in two dimensions the high-velocity instability occurs only for extreme crack velocities ($v_{cr} > 0.8c_R$), as the crack oscillates. This argument is based on experiments, in both biaxial mode-I cracks in rubber [23] and pure mode-I experiments in gels [24], and associated theoretical works [25,26]. However, the mode-I experiments in PMMA seem to indicate that beyond a certain crack velocity (especially right before macrobranches appear), the crack structure that emerges is essentially two dimensional, at least near the point where microbranches tend to create large macrobranches [7]. There has been some success in exploring the instability using phenomenological mesoscale approaches based on the phase field [27] or on cohesive zones [20,28–30]; these, however, are difficult to quantitatively relate to an underlying microscopic picture.

The failure of the continuum theory (LEFM) has given rise to an extensive theoretical effort using atomistic lattice

---

*kessler@dave.ph.biu.ac.il

models [31–41] and lattice simulations [33,34,38,40–47], where the inherent divergence of the elastic fields near the crack tip of the continuum theories is tamed, due to the finite atomistic lattice scale. These models yield steady-state cracks without any additional parameters, once the interatomic forces are specified. Both lattice models and simulations have shown and reproduced the sharp transition between steady-states cracks, where only the bonds on the midline of the lattice are broken, and the postinstability behavior, where beyond some critical velocity, other bonds start to fail. This critical velocity was found to have a strong dependence (with $0.3c_R < v_{cr} \leqslant c_R$) on the parameters of the potential, i.e., it is material dependent. Although the lattice models yield the desired existence of a critical velocity, regarding the postinstability point behavior, the success is much less impressive. While mode-III (out-of-plane shear mode) simulations have shown the existence of frustrated branching [33,38], similar mode-I simulations (the mode for which most of the experiments actually have been performed) have failed to reproduce the qualitative patterns of microbranches emerging near the main crack [40,42].

Accordingly, several attempts have been made to try to simulate cracks in amorphous materials, in which the bulk of experiments have been performed (e.g., glass, PMMA, and Homalite-100). Early attempts using the classic binary-alloy model (using two different kinds of particles) [48] to simulate an amorphous material failed [49–51]; the crack always arrested, due to the high mobility of dislocations, resulting in ductile behavior. Recently, Dauchot *et al.* [52] succeeded in generating propagating steady-state cracks using the binary-alloy model by going to the extreme brittle limit, where the force falls rapidly to zero for very small strains. However, no information was reported regarding the high-velocity instability. Moreover, the radial distribution function (RDF) $g(r)$ generated from the amorphous model presented in [52] is qualitatively different from the $g(r)$ of real amorphous materials.

A different direction was recently proposed [53], based on a continuous random network (CRN) model for simulating amorphous materials [54,55]. In this model the sample looks like a distorted lattice, while each atom shares the same number of nearest-neighbor atoms. The distortion is large enough to destroy the lattice peaks of the perfect crystal and the resulting RDF reproduces very well that of real amorphous materials, e.g., amorphous silicon. The CRN model yields both steady-state cracks and the main features of the microbranching instability, including the increasing size of the microbranches and the increasing oscillations in the electrical resistance of a metallic strip deposited on the surface of the sample (changes in resistance being correlated [7] to the crack velocity) [53] with increasing external loading. (In [53], using the CRN model, we noticed that there was no increase in the amplitude of the oscillations in the main-crack velocity, but there was a major increase in the amplitude of the oscillations in the electrical resistance, due to the birth of microbranches. Thus we prefer to use the terminology of electrical resistance rather than crack velocity in referring to the results of [7], etc.) Some works based on an elastic beam model [56,57] and the Born-Maxwell model [58–60] have shown progress in recovering some features of unstable mode-I fracture. However, these are mesoscopic, not microscopic, models;

the relationship between our work and these works will be analyzed in Sec. V.

In this work we focus on trying to reproduce the successful results of the CRN model also in lattices (where previous attempts have failed, as explained above). We hypothesize that the basic phenomenology of the CRN is due in large measure to the inherent randomness present in the model. Thus we introduce a degree of randomness into a standard lattice model, letting the force law between the atoms vary slightly by changing randomly the lattice scale a between the atoms. As a result, the equilibrium locations of the atoms are slightly changed from their pure lattice locations, according to the modified force law. By breaking the perfect symmetry of the original lattice, we will see that it is possible to obtain a realistic microbranching phenomenon in these simple structures.

This approach has a number of advantages over the CRN method. First, it is computationally cheaper and it is not necessary to first create and equilibrate a CRN sample. Second, the system should be much less noisy, reducing the amount of averaging (as well as the observation scale) required for quantitative characterization. In addition, from a theoretical viewpoint, it is interesting to determine to what extent the structural disorder present in the CRN, but not in the current noisy lattice model, is essential for realistic microbranching.

II. MODEL AND MAIN METHODOLOGY

In our model, each bond (between atoms i and j) has a specific characteristic equilibrium distance at which the force is zero. This distance $a_{i,j}$ is taken to vary slightly from the constant distance a_0 by a factor of $\epsilon_{i,j}$, which is drawn from a uniform distribution:

$$a_{i,j} = (1 + \epsilon_{i,j})a_0, \quad i = 1,2,\ldots,n_{\text{atoms}}, \ j \in \mathcal{N}(i), \quad (1)$$

where $\epsilon_{ij} \in [-b,b]$ (b is a constant for a given lattice and in this work is in the range $0 \leqslant b \leqslant 0.1$), $a_0 = 4$, and $\mathcal{N}(i)$ refers to the nearest neighbors of site i.

Between each two atoms there is a piecewise-linear radial force (two-body force law) of the form

$$\vec{f}_{i,j}^R = k_R(|\vec{r}_{i,j}| - a_{i,j})\theta_H(\varepsilon - |\vec{r}_{i,j}|)\hat{r}_{j,i}, \quad (2)$$

where the Heaviside step function θ_H guarantees that the force drops immediately to zero when the distance between two atoms $|\vec{r}_{i,j}|$ reaches a certain value $\varepsilon > a_{i,j}$ (the breaking of a
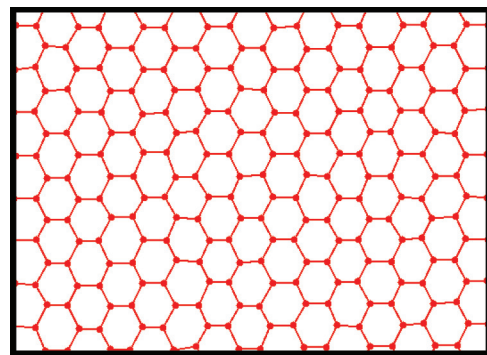

FIG. 1. (Color online) Typical steady-state perturbed-lattice grid using $b = 10\%$.
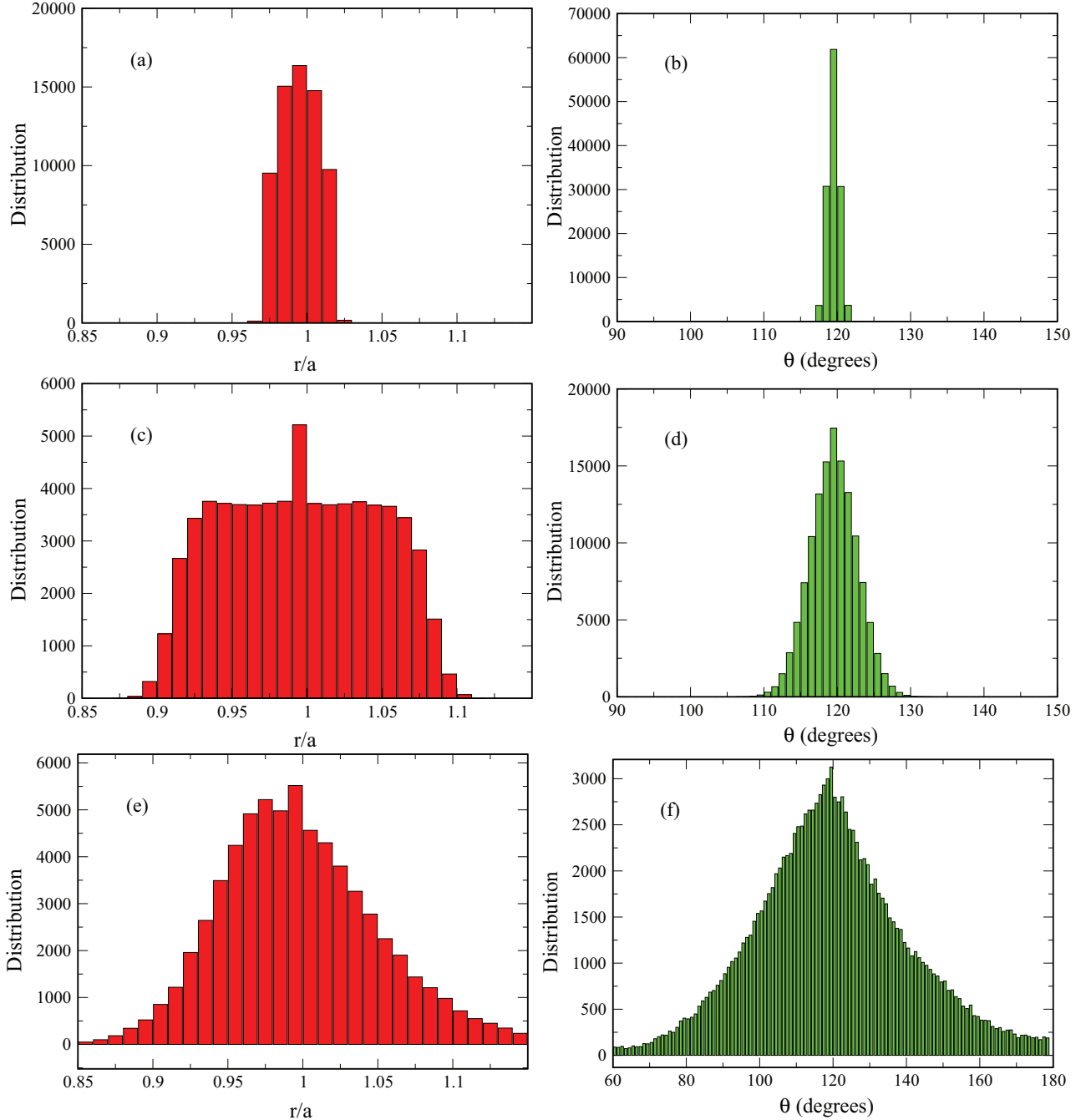
FIG. 2. (Color online) (a) Radial and (b) angular distributions for a perturbed-lattice mesh with $b = 2.5\%$. (c) Radial and (d) angular distributions for a perturbed-lattice mesh for $b = 10\%$. (e) Radial and (f) angular distributions for the CRN amorphous mesh.

bond). In this work we set $\varepsilon = a_0 + 1$ and the units are chosen so that the spring constant k_R is unity. Potentially, in addition there is a three-body force law that depends on the cosine of each of the angles, defined of course by

$$\cos\theta_{i,j,k} = \frac{\vec{r}_{i,j} \cdot \vec{r}_{i,k}}{|\vec{r}_{i,j}||\vec{r}_{i,k}|}. \tag{3}$$

In a honeycomb lattice there are three angles associated with each atom and in the hexagonal lattice there are six of them (we note that in the hexagonal lattice this choice is a little bit arbitrary since there are in general additional optional angles for each atom). There is a certain preferred angle θ_C for which

the three-body force law vanishes (in the honeycomb lattice we set $\theta_C = 2\pi/3$ and in the hexagonal lattice we set $\theta_C = \pi/3$). The three-body force law that acts on the central atom (atom i) of each angle may be expressed as

$$\vec{f}_{i,(j,k)}^{\theta} = k_\theta(\cos\theta_{i,j,k} - \cos\theta_C)\frac{\partial \cos\theta_{i,j,k}}{\partial \vec{r}_i}\theta_H(\varepsilon - |\vec{r}_{i,j}|)\hat{r}_i$$

$$= k_\theta(\cos\theta_{i,j,k} - \cos\theta_C)\left[\frac{\vec{r}_{i,j} + \vec{r}_{i,k}}{|\vec{r}_{i,j}||\vec{r}_{i,k}|} + \frac{\vec{r}_{j,i}(\vec{r}_{i,j} \cdot \vec{r}_{i,k})}{|\vec{r}_{i,j}|^3|\vec{r}_{i,k}|}\right.$$

$$\left. + \frac{\vec{r}_{k,i}(\vec{r}_{i,j} \cdot \vec{r}_{i,k})}{|\vec{r}_{i,j}||\vec{r}_{i,k}|^3}\right]\theta_H(\varepsilon - |\vec{r}_{i,j}|), \tag{4}$$
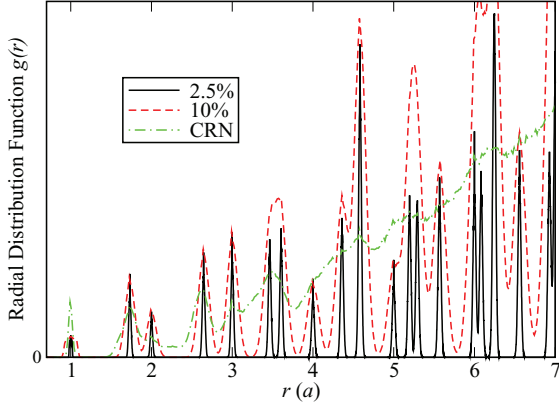
FIG. 3. (Color online) Radial distribution function $g(r)$ as a function of r (in lattice scale units) in the perturbed-lattice systems with different magnitude and in the continuous random network system. A major qualitative difference can be seen between the two networks.

while the force that is applied on the other two atoms (atoms j and k) may be expressed as

$$\vec{f}^{\theta}_{j,(i,k)} = k_{\theta}(\cos\theta_{i,j,k} - \cos\theta_C)\frac{\partial\cos\theta_{i,j,k}}{\partial\vec{r}_j}\theta_H(\varepsilon - |\vec{r}_{i,j}|)\hat{r}_j$$

$$= k_{\theta}(\cos\theta_{i,j,k} - \cos\theta_C)\left[\frac{\vec{r}_{k,i}}{|\vec{r}_{i,j}||\vec{r}_{i,k}|} + \frac{\vec{r}_{i,j}(\vec{r}_{i,j}\cdot\vec{r}_{i,k})}{|\vec{r}_{i,j}|^3|\vec{r}_{i,k}|}\right]$$

$$\times \theta_H(\varepsilon - |\vec{r}_{i,j}|). \quad (5)$$

Of course, the forces satisfy the relation $\vec{f}^{\theta}_{i,(j,k)} = -(\vec{f}^{\theta}_{j,(i,k)} + \vec{f}^{\theta}_{k,(i,j)})$.

In addition, it is convenient to use a Kelvin-type viscoelastic force [35] proportional to the relative velocity between the two atoms of the bond $\vec{v}_{i,j}$:

$$\vec{g}^{R}_{i,j} = \eta(\vec{v}_{i,j}\cdot\hat{r}_{i,j})\theta_H(\varepsilon - |\vec{r}_{i,j}|)\hat{r}_{i,j}, \quad (6)$$

with η the viscosity parameter. The viscous force vanishes after the bond is broken. The imposition of a small amount of such a viscosity acts to stabilize the system and is especially useful in the relatively narrow systems simulated herein.

The equation of motion of each atom is then

$$m_i\vec{a}_i = \sum_{j\in\mathcal{N}(i)}\left(\vec{f}^{R}_{i,j} + \vec{g}^{R}_{i,j}\right) + \sum_{j,k\in\mathcal{N}(i)}\vec{f}^{\theta}_{i,(j,k)} + \sum_{\substack{j\in\mathcal{N}(i),\\k\in\mathcal{N}(j)}}\vec{f}^{\theta}_{j,(i,k)}, \quad (7)$$

where there are 3 terms in the second sum and 6 terms in the last sum for the honeycomb lattice and 6 and 12 terms
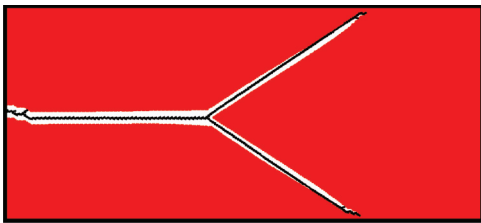

FIG. 4. (Color online) Propagating crack snapshot using a pure honeycomb lattice using $\eta = 0.25$ and $\Delta/\Delta_G = 2.7$. The crack bifurcates into two branches that then travel to the end of the sample.

respectively for the hexagonal lattice. The masses m_i can also be set to unity without loss of generality.

The main methodology is as follows: After choosing the random value $a_{i,j}$ for each bond, we allow the network to relax through a simple molecular-dynamics Euler scheme, in accord with Eq. (7), with a nonzero η, until the total energy is minimized. In Fig. 1 we can see an example of a perturbed honeycomb lattice with $b = 10\%$, while in Fig. 2 we can see the distribution of the radial distances of the bonds for a perturbed lattice with $b = 2.5\%$ and 10% along with the CRN, taken from [53], along with the distribution of bond angles.

We can see the qualitative difference between the perturbed-lattice mesh and the CRN. While the radial distributions for the perturbed-lattice mesh are flat in the range of $1 \pm b$ and then drop immediately to zero (since the random distribution was taken to be flat in the range of $1 \pm b$), that for the CRN has a long tail extending over larger distances. In addition, the angular distributions are much narrower than the CRN's angular distribution.

A powerful tool to check the character of the grid is the RDF. In Fig. 3 we can see the RDFs of the perturbed lattices and the CRN. We can see again the qualitative difference between the meshes. While the CRN looks very much like a real amorphous material (see [53]), the RDFs of the perturbed lattices look exactly like a pure lattice RDF (set of δ functions), only slightly perturbed due to the random noise, even for large r. Thus the structure of the perturbed lattices is more like a lattice material rather than an amorphous material.

After relaxing the initial lattice, we strain the lattice under a mode-I tensile loading with a given constant strain using a given driving displacement Δ and seed the system with an initial crack. We let the crack propagate via the same molecular-dynamics Euler scheme using Eqs. (2)–(7). The lattice mesh we use contains $162 \times 272 \approx 45\,000$ ($N = 80$ in the Slepyan model notation) atoms for the honeycomb lattice and $162 \times 408 \approx 65\,000$ atoms for the hexagonal lattice.

We note that because of the relatively small size of the lattice we use a large value of η in our honeycomb-lattice simulation to keep the propagating crack in the middle of the sample. As a result, we need huge values of Δ/Δ_G for the crack to propagate. This is a numerical artifact, while in larger (physical) samples, η can be taken much smaller and the value of Δ/Δ_G is more physical. However, the main features are nevertheless quite similar. In addition, in the hexagonal lattice (see Sec. IV), we indeed use small values of η and the values of Δ/Δ_G are more realistic.

III. HONEYCOMB LATTICE

Using $b = 0$, i.e., an unperturbed honeycomb lattice, we obtain the well-known cleaving behavior (characterizing crystalline materials) of the crack above threshold. For small strains we get a perfect steady-state crack, while upon increasing the driving displacement, the crack bifurcates to two macrobranches that propagate to the edges of the sample [40]. The same happens in the honeycomb lattice including the three-body force law, both with a large viscosity and with a negligible viscosity (Fig. 4).

Using a finite value of b to perturb the lattice, we obtain nice snapshots of microbranches, very much like those obtained
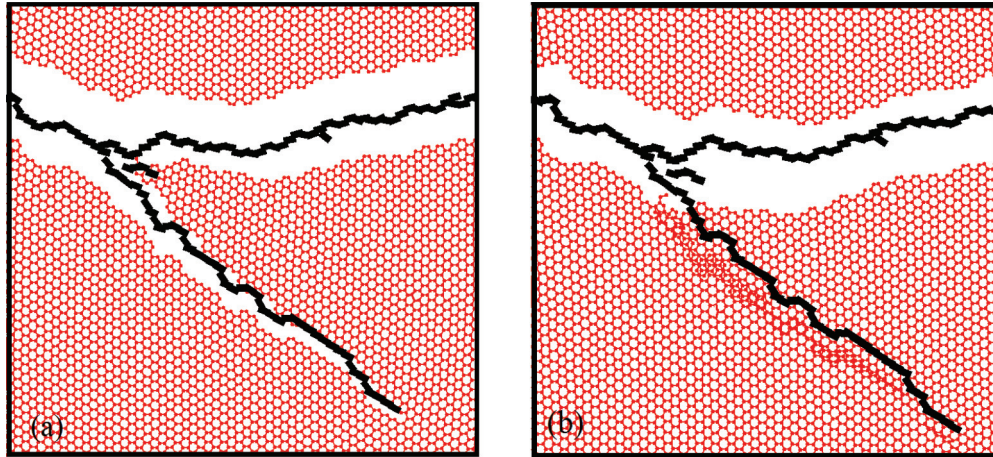
FIG. 5. (Color online) (a) Snapshot of a propagating crack using a perturbed-honeycomb-lattice model using $b = 10\%$, $\eta = 2$, and $\Delta/\Delta_G = 3.8$. (b) Snapshot of the overlapping problem. After cracking, the two pieces of the cracked-lattice overlap because bond breakage is an irreversible process in this model. We note that the length of the largest microbranches is approximately 50 broken bonds, i.e., we checked that the branches do not correlate with the end of the sample.

using the CRN [53]. In Fig. 5(a) we can see that when the driving displacement exceeds some value, a large microbranch starts to appear. In Fig. 6 we can see the final pattern of broken bonds for two cases, one for $\eta = 2$ [Fig. 6(a)] and one for $\eta = 2.5$ [Fig. 6(b)]. The patterns looks very much like the fracture pattern seen using the CRN. Moreover, the microbranches also look similar to the experimental images of microbranches in PMMA [5–10]. This is an important result because in this model such a microbranch pattern appears in a lattice material using fully 2D atomistic simulations (previously shown by us using an amorphous material model [53]). For further analysis on the difference between this current work and previous works (for example, [29,56–60]), see Sec. V. We note that when the main crack continues and the microbranch arrests, one piece of the lattice overlaps with another piece [see Fig. 5(b)]. This is a nonphysical effect and is caused by the fact that bond breakage in this model is irreversible. This effect is not large using the honeycomb lattice, but will be much more pronounced for the hexagonal lattice.

Beyond obtaining the qualitative features of the micro-branches, the perturbed-lattice model reproduces the main semiquantitative results of mode-I fracture beyond the onset of instability. Because of the chaotic nature of the problem (small changes in the simulation parameters yield different crack patterns, but with similar quantitative properties, such as the crack velocity), we changed the time step by a little bit ($\pm 15\%$)

for each driving displacement Δ to have sufficiently good statistics on the resulting measurements [about 20 runs for each point, therefore, each point in Figs. 7(a)–7(c) represents an average over $\approx$20 runs]. In Fig. 7 we can see (a) the $v(\Delta)$ curve, (b) the total length of the microbranches, and (c) the amplitude of the oscillations of the electrical resistance, which is correlated [7] to the crack velocity.

The $v(\Delta)$ curve looks very much like the typical $v(\Delta)$ curve for mode-I fracture (for example, see [40,41,53]). The error bars represent the statistical error of the crack's velocity using several simulations for each Δ. The graph of the total length of the microbranches as a function of the crack's velocity is one of the most important results of this work. We can easily see that the total length of microbranches goes to zero at small velocities, with a clear growth (near $v \approx 0.57c_R$) with increasing velocity (or Δ). This is in direct accord with the experimental results (but instead of a sharp transition between the steady-state cracks' area and microbranches' area, we get a smooth transition due to the noisy character of discrete atomistic simulation at smaller scales). Actually, the experimental results refer to the length of an average single microbranch, but because the lack of statistics (we have only a few microbranches in each single simulation, so it is hard to define the length of an average single microbranch), we use the total sum of broken bonds instead (besides, of course, the main crack). This should be a sufficiently close substitute
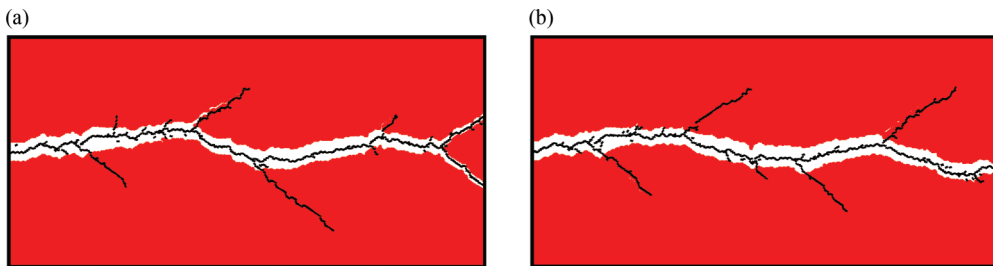

FIG. 6. (Color online) (a) Pattern of the final cracked lattice using a perturbed-honeycomb-lattice model using $b = 10\%$, $\eta = 2$, and $\Delta/\Delta_G = 3.8$. (b) Same as (a) but with $\eta = 2.5$ and $\Delta/\Delta_G = 4$.
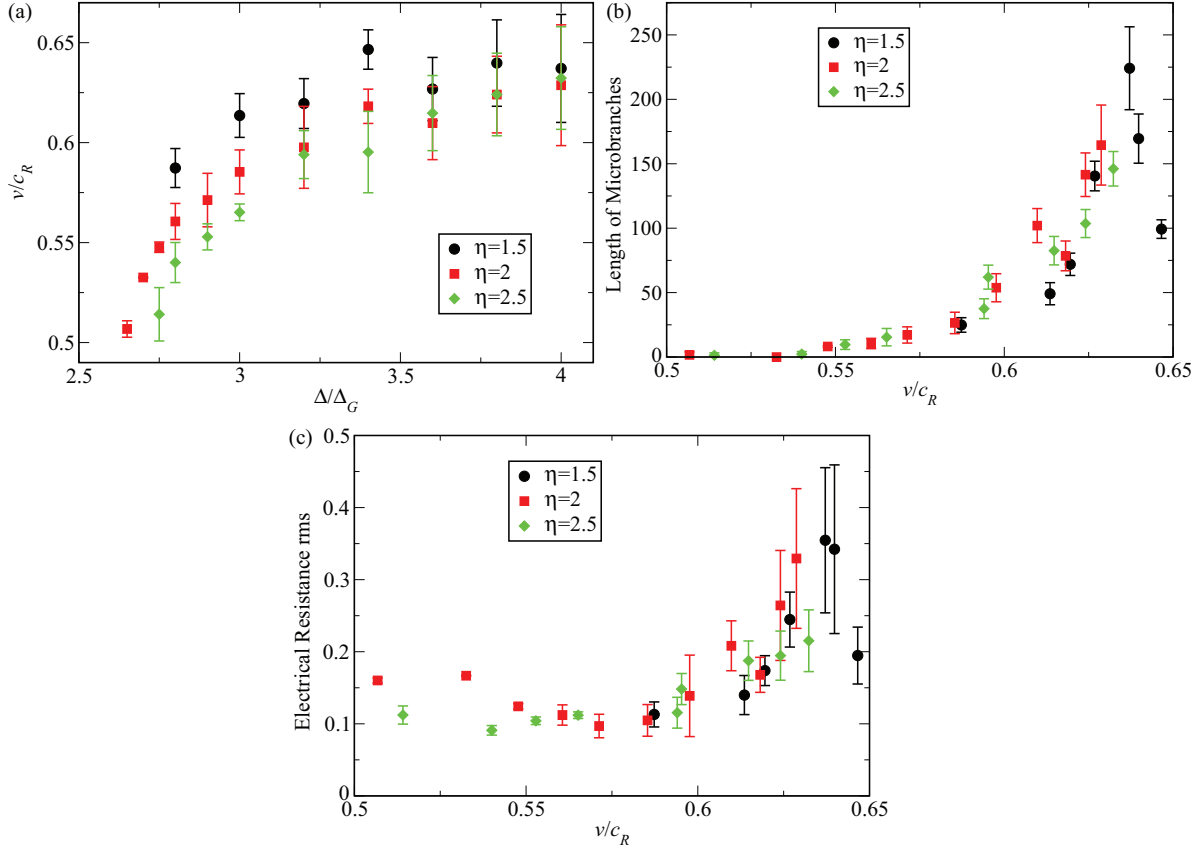
FIG. 7. (Color online) (a) The $v(\Delta)$ curves measured from simulations of the perturbed honeycomb lattice model using $b = 10\%$ with different η. The error bars were calculated using several simulations, each with a small change in dt, exploiting the chaotic nature of the problem. (b) Size of the total number of microbranches as a function of the crack velocity v. For small velocities the total size of microbranches tends to zero (a steady-state crack). (c) Amplitude of the oscillations in the electrical resistance as a function of the crack velocity. Even in steady-state cracks, the amplitude of the oscillations tends to a certain finite (nonzero) value.

(we see that we do not have just more short microbranches at large drivings; the size of each microbranch indeed grows). Compared to the corresponding result using the CRN for amorphous material [53] [see also the triangles in Fig. 8(b)], where this transition was not very pronounced, here it is much clearer. We note that in defining the total size of the microbranches we subtracted all the microbranches of the size of one or two broken bonds, which we neglect and treat as numerical noise.

From Fig. 7(b) we can see that using $\eta = 1.5$ yields a very noisy system and we get either arrested cracks at small driving or significant microbranching (at larger Δ). There is no intermediate zone of steady-state cracks. Only after increasing the dissipation to $\eta = 2$ do we obtain clear steady-state cracks. Increasing η further to $\eta = 2.5$ does not change the results appreciably. In addition, the amplitude of the oscillations of the electrical resistance shows qualitative agreement with the experimental results, as well as the CRN results [53]. (For an in-depth discussion of the different terminology between the crack's velocity oscillation and the electrical resistance oscillations and the appropriateness of the latter as a diagnostic, see [53].) Beyond the critical velocity for steady-state cracks, the amplitude of the oscillations increases rapidly, while for smaller velocities the amplitude of the oscillations is constant.

The sensitivity to the value of b, characterizing the width of the bond length distribution, was also investigated, exploring how much we can reduce b and still get a similar micro-branching pattern, recalling that $b = 0$ (pure lattice) creates a cleaving pattern characteristic of crystalline materials. For $b \lesssim 1\%$, the system exhibits pure cleaving behavior, i.e., the perfect lattice behavior is not a singular case, and the cleaving pattern is stable to infinitesimal changes in the lattice and does not produce microbranches. A significant perturbation is needed to yield microbranching behavior. In fact, even for $b = 2.5\%$, the microbranches seems to propagate almost along straight lines, along the preferred lattice directions, and thus are still strongly influenced by the lattice. In Fig. 8 we show the quantitative results using different values of b, along with the CRN results (taken from [53]).

From the $v(\Delta)$ curve [Fig. 8(a)] and the amplitude of the oscillations [Fig. 8(c)] we can see that the CRN is closest to the $b = 10\%$ results. In Fig. 8(b), for the length of the microbranches, we see the CRN results most resemble the low-b results. This fact encourages us to conclude that the transition seen in the CRN between low velocities and high, although rounded, is nevertheless real since in the current model increasing b yields qualitatively similar results, but with a more distinct transition. It is important to note that the point of instability is b dependent, i.e., material dependent. For
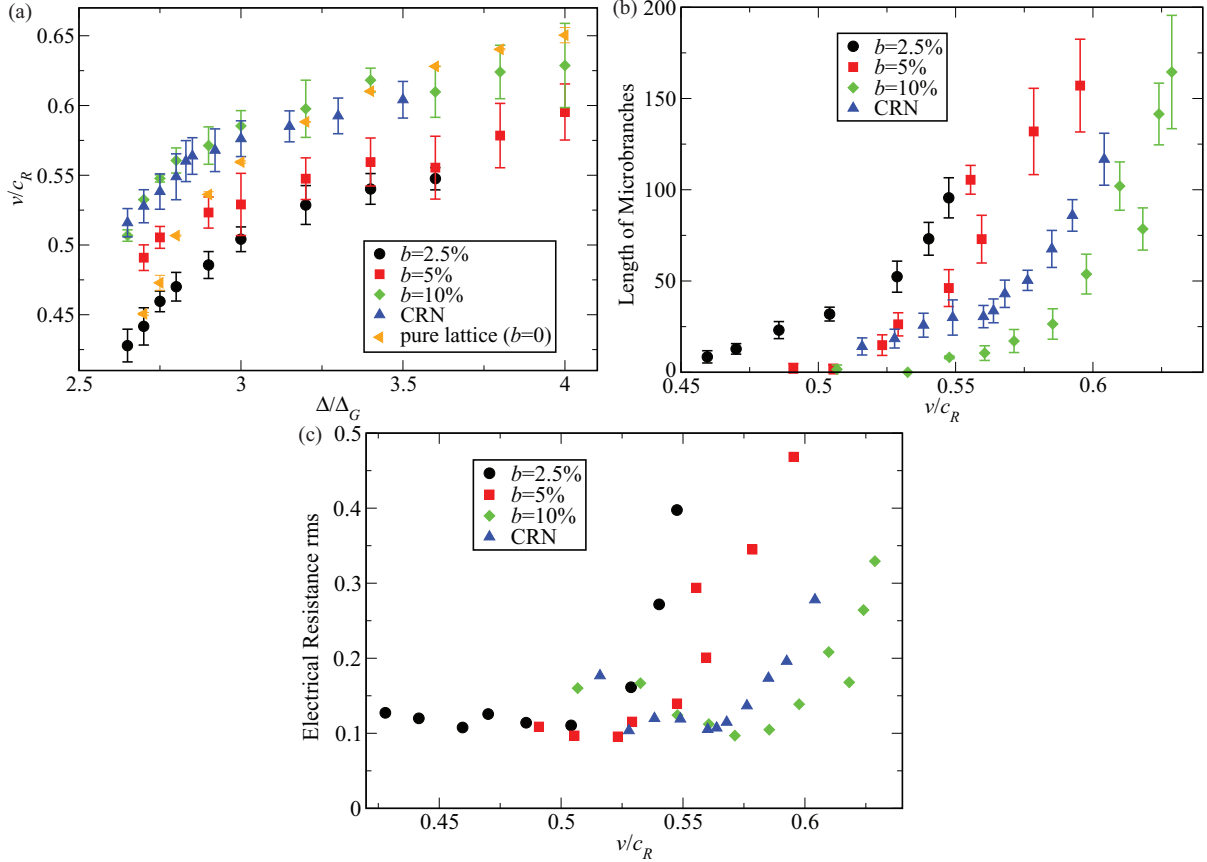
FIG. 8. (Color online) (a) Resulting $v(\Delta)$ curve for a perturbed-honeycomb-lattice model with different values of b (including $b = 0$, a perfect lattice), along with the CRN results (taken from [53]) using $\eta = 2$. The CRN curve is closer to the $b = 10\%$ curve. (b) Size of the total number of microbranches as a function of the crack velocity v. The somewhat questionable transition between steady-state cracks and microbranch behavior using the CRN looks much more clear using perturbed-lattice models. (c) Amplitude of the oscillations in the electrical resistance as a function of the crack velocity. Again, the CRN curve is closer to the $b = 10\%$ curve.

$b = 2.5\%$ the critical velocity is approximately $0.45c_R$ (which is by chance consistent with the experiments), while for larger b it approaches $0.57c_R$. However, plotting Fig. 8(b) as a function of Δ yields an approximately constant $\Delta_{cr} \approx 2.75\Delta_G$. The pure lattice shows a very different behavior. The slope of the $v(\Delta)$ curve is much sharper and the point of instability is around $\Delta_{cr} \approx 3.6\Delta_G$ (nonmicrobranching behavior).

IV. HEXAGONAL LATTICE

The classic lattice dynamical fracture simulations in perfect lattices used a hexagonal lattice [33,34,39–42,44,46,47]. As mentioned in the Introduction, those models exhibited frustrated branching in the mode-III fracture simulations [33,38], but failed to recreate the experimentally observed [40,42] pattern of microbranches in mode-I fracture simulations. The idea of trying to induce microbranching via introducing noise into the interatomic potential was an obvious possibility to try. However, the initial round of attempts in this direction did not succeed [61]. The findings from the preceding section, that a relatively small perturbation in the potential between the atoms can create a more realistic pattern of mode-I fracture, raises the question of why these previous models failed while our

current model succeeded. The key, it turns out, lies in the use of the three-body force. Such a force is in any case essential in the honeycomb lattice in order to stabilize the lattice. In the hexagonal lattice, however, such a force is not required in general and, given its computation expense, was typically not included in the model. While not required for the stability of the lattice, it appears, as we shall see, that it is in general necessary to achieve realistic microbranching.

We first present the results for a perturbed hexagonal lattice without a three-body force (i.e., $k_\theta = 0$). The radial and angular distributions are shown in Fig. 9. Using the same magnitude of perturbation as in the honeycomb lattice, $b = 10\%$ yields an extremely noisy simulation and eventually, in most cases, the crack arrests. Using a smaller value of b ($b = 2.5\%$) yields microbranching patterns for large driving displacement, but as can be seen in Fig. 10(a), the microbranches tend to propagate straight ahead and to exhibit intermittent bond breaking, neither of which is desirable. Occasionally, however, more realistic branching does occur, as exemplified in Fig. 10(b). At low drivings, as expected, there is a single steady-state crack propagating in the midline of the sample with no broken bonds besides the main crack. Using b smaller than 2.5% reproduces the cleaving behavior of crystalline materials.
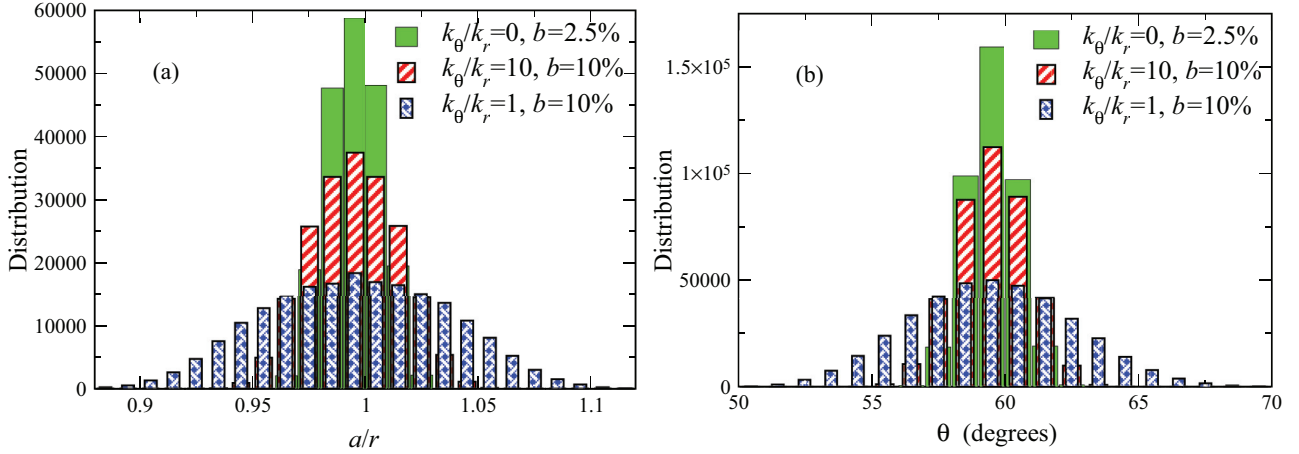
FIG. 9. (Color online) (a) Radial and (b) angular distributions for a perturbed-hexagonal-lattice mesh with and without three-body force law using different values of b. Here $k_\theta/k_r = 1$ and $b = 10\%$ yield almost the same distributions as $k_\theta/k_r = 0$ and $b = 10\%$ do.

Despite the unphysical microbranching typically exhibited by the model without the three-body force law, it is nevertheless a useful benchmark system since it can be compared to Slepyan's lattice steady-state models (like in [40], using large α, which corresponds to a piecewise-linear model) in which the origin of instability between steady-state cracks and microbranches behavior is known exactly (although the models use $b = 0$, the small perturbation does not change the results significantly).

The quantitative results regarding the $v(\Delta)$ curve and the total size of microbranches as a function of v are presented in Fig. 11. We can see in Fig. 11(a) that the velocities below $v = c_R$ reproduce Slepyan's lattice model results from [40], yielding perfect steady-state cracks, with no microbranches at all [Fig. 11(b)]. Increasing the driving displacement Δ further yields a non-steady-state behavior, as the steady-state lattice model solution becomes unstable, yielding a microbranching behavior (again, only above a threshold b). The crack velocities are higher than c_R for large Δ. This is an artifact due to the relatively small size of the sample (see, for example, Sec. VI in [35]). The problem of overlapping zones is more extensive in the hexagonal lattice (with and without the three-body force) [see Fig. 12], yielding large areas of overlapping zones, which is again unphysical. The main benefit so far of using this model is that Fig. 11(b) yields qualitative results similar to those in Fig. 7(b) or 8(b), emphasizing that the transition at low velocities to a steady-state behavior is real since in a hexagonal case we get absolutely zero microbranches at low velocities, and agreement with Slepyan's lattice models. In

addition, the hexagonal mesh allows us to work with small values of η, which is more relevant experimentally [62,63] than the large-η honeycomb lattice.

Adding a three-body force law in a hexagonal lattice, one must use large values of k_θ since the relatively large number of nearest neighbors does not allow each group of three atoms to generate an angle significantly larger than $\pi/3$ using $k_\theta \approx k_r$ (as was the case in the honeycomb lattice) and thus the three-body energy is negligible. When we increase k_θ using $b = 2.5\%$, we have perfect lattice behavior because k_θ is too large. Increasing b further to $b = 10\%$ yields a good balance where the three-body energy is not negligible and radial and angular distributions similar to that of the hexagonal lattice without the three-body force law using $b = 2.5\%$ (see Fig. 9).

We normalize the $v(\Delta)$ curve results and the total size of microbranches as a function of v using this model to the values of the non-three-body force law case (see the caption to Fig. 11) and present them in Fig. 11. We can see that these two models share the same qualitative behavior (although including the three-body force law results in a small number of microbranches at low velocities, very much like the honeycomb case). In addition, this model still suffers from a severe problem of overlapping of pieces of the mesh after branching (in contrast to the honeycomb lattice, where this problem is minor), as can be seen in Fig. 12.

However, two surprising results appear using this model (a perturbed hexagonal lattice including three-body force law). First, the main crack stays more confined to the middle of the sample, even for large driving (within $\approx 10\%$ from the total
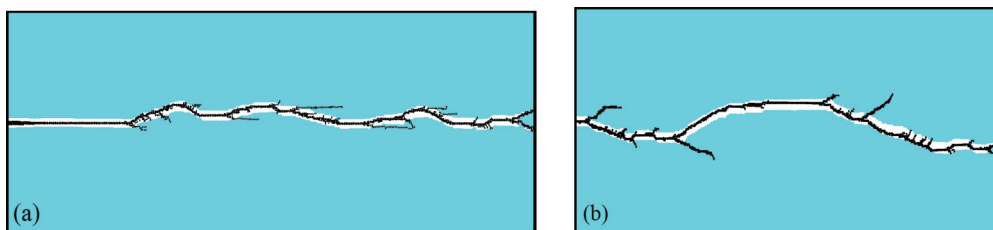

FIG. 10. (Color online) Two examples of the final cracked lattice using a perturbed-hexagonal-lattice (without three-body forces) model using $b = 2.5\%$, $\eta = 0.25$, and $\Delta/\Delta_G = 2.2$, with slightly different values of dt.
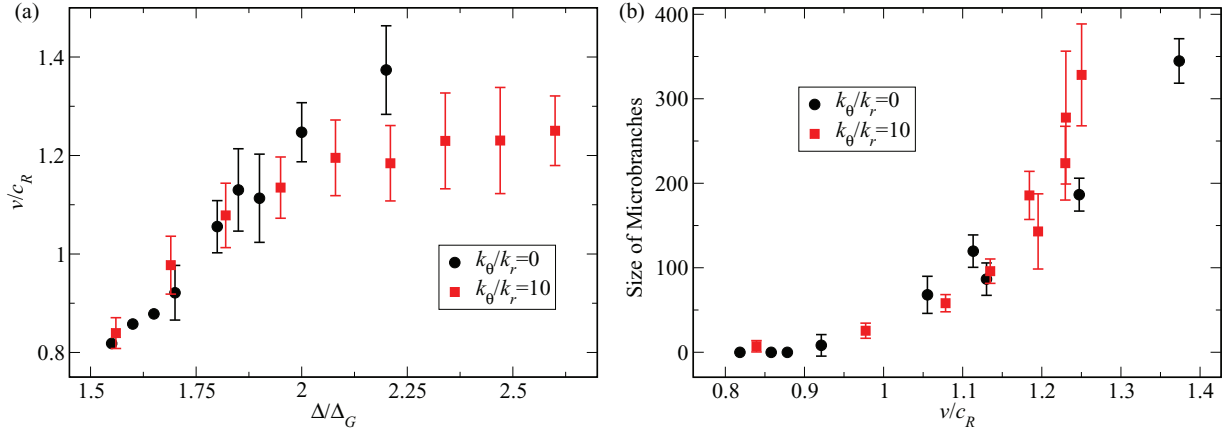
FIG. 11. (Color online) (a) Resulting $v(\Delta)$ curve for a perturbed-hexagonal-lattice model using different values of k_θ with $\eta = 0.25$ ($b = 2.5\%$ for $k_\theta/k_r = 0$ and $b = 10\%$ for $k_\theta/k_r = 10$). The error bars were calculated using several simulations, each with a small change in dt, due to the random nature of the problem. (b) Size of the total number of microbranches as a function of the crack's velocity v. In small velocities the total size of microbranches tends to zero (a steady-state crack). The results with the three-body force included are normalized to the non-three-body results (because the three-body force law is dominant here, $k_\theta/k_r = 10$, c_R and Δ_G are harder to estimate, and since we are interested in the qualitative shapes of the curves, we simply normalize both v and Δ to share values similar to those in the pure two-body problem).

width of the sample for large Δ), with large microbranches, in contrast to all other models, including the honeycomb-lattice model (within $\approx 25\%$ from the total width of the sample for large Δ). Second, and most important, the larger microbranches have a nonlinear power-law shape very much like the experimental data. In Fig. 13 we can see several crack patterns for different driving displacements (with different dt, with shifting in the y axis). We add a basic power-law fit (with different x_0 and y_0 for each large microbranch). We get a fairly clean power-law behavior (but with an exponent of 0.5–0.65 instead of the ≈ 0.7 of [5,7]). This is of course a very preliminary result and must be tested in larger-scale systems.

We note that macroscopic cracks often propagate in straight lines [2,10], so the physical behavior of Figs. 6 and 10 is important too, especially given that the experiments are two dimensional near the onset of macrocracks (see Sec. V for
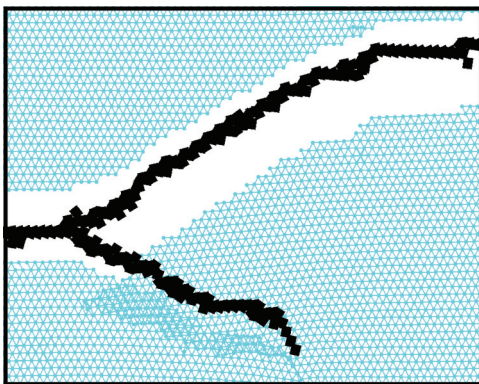

FIG. 12. (Color online) Snapshot showing the extensive overlapping problem. This figure is a blowup of the branching event in Fig. 10(b). Similar pictures are obtained in the presence of the three-body force. After cracking, the two pieces of the cracked-lattice overlap because fracture is irreversible process in this model.

further details). Power-law behavior (different from 1) is seen in the atomistic model only in a perturbed hexagonal lattice including three-body force law. These observations support the conclusion that the macroscopic behavior of fracture depends strongly on the interatomic microscopic potential.

V. DISCUSSION

We have shown that microbranching can be reproduced in lattice materials in molecular-dynamic microscopic simulations, using a small perturbation parameter b (but larger than a critical value of $\sim 1\%$) that perturbs the interatomic potential. Among the parameters considered in this work, this disorder is the key component that is responsible for producing a semirealistic pattern of microbranches, in contrast to the very different behavior of cleaving fracture of perfect lattices. Such microbranching behavior is seen in both honeycomb and hexagonal lattices with a three-body force and to a much more limited extent also in the hexagonal lattice without a three-body force law. In addition to the qualitative patterns of microbranches, semiquantitative results are shown, particularly the total length of microbranches (which corresponds to the average size of a microbranch in the experiments) as a function of the velocity. A clear transition between steady-state behavior and the postinstability region is seen, characterized by an increased number of broken bonds off the midline of the sample. This result is in line with the results of the CRN model. The transition is clearest in the case of the hexagonal lattice without the three-body force law, where for small driving there is absolutely no microbranching at all, as in the unperturbed-lattice models. The increased amplitude of the rms of the electrical resistance is shown as well, in agreement with the experiments. The viscosity (defined by the parameter η) was used for numerical convenience only, because of the finite size of the samples studied. The main results remain the same when decreasing η, as the hexagonal-lattice results indeed show. In addition, preliminary signs of power-law
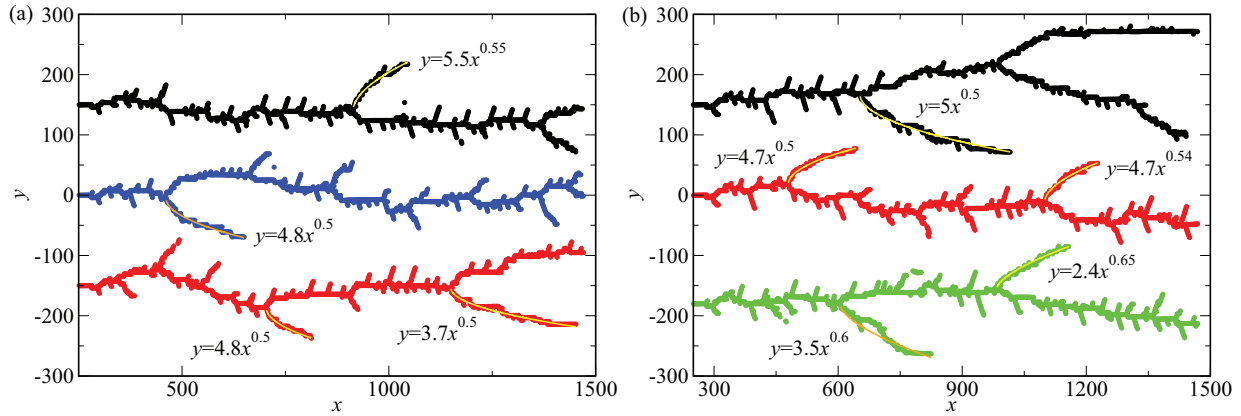
FIG. 13. (Color online) Crack pattern for a perturbed-hexagonal-lattice model using $k_\theta/k_r = 10$, $b = 10\%$, $\eta = 0.25$, and (a) $\Delta/\Delta_G = 1.8$ with different values of dt and (b) $\Delta/\Delta_G = 1.9$ with different values of dt for the top and middle patterns and $\Delta/\Delta_G = 2$ for the bottom pattern.

behavior for the shape of the side branches can be seen using a hexagonal lattice including a three-body force law, in accord with experiment.

As mentioned in the Introduction, several features of mode-I fracture were found in various models before. The distinctive aspect of our simulations is that they are pure 2D atomistic simulations with specified forces between the atoms (with or without three-body force law), while the atoms are free to travel to any direction in the sample. In contrast, the works of Astrom *et al.* [56,57] based on elastic beams and the works of Heino and Kaski [58–60] based on the Born-Maxwell model (with and without disorder) separate the force law between the atoms into two parts, a central one and a bending term, which penalize rotation of the springs away from lattice directions, yielding a nonrotationally invariant behavior [64] (this bending term is an alternative to using a three-body force term; see [64]). In addition, the microbranching of both [56,57] is affected dramatically by the lattice shape and thus is nonphysical. In [58], again the branching is symmetric in the y direction, in contrast to experimental results. The pattern of [59] looks more physical. All of these works did not yield evidence of the increase in size of the branches as seen in Fig. 8 or 12. Patterns of microbranches using finite-element methods are common in the work of many

groups (for example, [20,29,30]), but they do not share the discrete (nonsingular) nature of our microscopic model.

We found once again that the macroscopic features of the dynamic fracture process, such as the critical velocity, is dependent on the microscopic parameters of the interatomic potential, i.e., material dependent. As mentioned in the Introduction, the universality of the critical velocity for creating microbranches is disputed. However, the critical velocity for creating macrobranches is for sure material dependent. Since the experiments show that the transition from 3D to 2D patterns is right before the microbranches tend to create macro-branches, and this point is strongly material dependent, it may not be surprising that in all out 2D simulations, we get a strong dependence on the material parameters. Much more extensive work is needed to extend this result to larger scales as well as exploring the opening angle of the crack.

ACKNOWLEDGMENTS

[1] K. Ravi-Chandar and W. G. Knauss, Int. J. Fract. **26**, 141 (1984).

[2] M. Ramulu and A. S. Kobayashi, Int. J. Fract. **27**, 187 (1985).

[3] J. Fineberg, S. P. Gross, M. Marder, and H. L. Swinney, Phys. Rev. Lett. **67**, 457 (1991).

[4] J. Fineberg, S. P. Gross, M. Marder, and H. L. Swinney, Phys. Rev. B **45**, 5146 (1992).

[5] E. Sharon, S. P. Gross, and J. Fineberg, Phys. Rev. Lett. **74**, 5096 (1995).

[6] E. Sharon, S. P. Gross, and J. Fineberg, Phys. Rev. Lett. **76**, 2117 (1996).

[7] E. Sharon and J. Fineberg, Phys. Rev. B **54**, 7128 (1996).

[8] E. Sharon and J. Fineberg, Philos. Mag. B **78**, 243 (1998).

[9] E. Sharon and J. Fineberg, Nature (London) **397**, 333 (1999).

[10] E. Sharon and J. Fineberg, Adv. Eng. Mater. **1**, 119 (1999).

[11] J. A. Hauch, D. Holland, M. P. Marder, and H. L. Swinney, Phys. Rev. Lett. **82**, 3823 (1999).

[12] K. H. Nam, I. H. Park, and S. H. Ko, Nature (London) **485**, 11002 (2012).

[13] J. Fineberg and M. Marder, Phys. Rep. **313**, 2 (1999).

[14] L. B. Freund, *Dynamic Fracture Mechanics* (Cambridge University Press, Cambridge, 1998).

[15] E. H. Yoffe, Philos. Mag. **42**, 739 (1951).

[16] J. D. Eshelby, Sci. Prog. **59**, 161 (1971).

[17] M. Adda-Bedia, J. Mech. Phys. Solids **53**, 227 (2005).

[18] A. Livne, G. Cohen, and J. Fineberg, Phys. Rev. Lett. **94**, 224301 (2005).

[19] A. Sagy, G. Cohen, Z. Reches, and J. Fineberg, J. Geophys. Res. **111**, B04406 (2006).

[20] M. Murphy and A. Ivankovic, Eng. Fract. Mech. **72**, 861 (2005).

[21] E. Bouchbinder, J. Mathiesen, and I. Procaccia, Phys. Rev. E **71**, 056118 (2005).

[22] E. Bouchbinder and I. Procaccia, Phys. Rev. E **72**, 055103(R) (2005).

[23] R. D. Deegan, P. J. Petersan, M. Marder, and H. L. Swinney, Phys. Rev. Lett. **88**, 014304 (2001).

[24] A. Livne, O. Ben-David, and J. Fineberg, Phys. Rev. Lett. **98**, 124301 (2007).

[25] E. Bouchbinder and I. Procaccia, Phys. Rev. Lett. **98**, 124302 (2007).

[26] E. Bouchbinder, Phys. Rev. Lett. **103**, 164301 (2009).

[27] H. Henry, Europhys. Lett. **83**, 16004 (2008).

[28] A. Raina and C. Linder, Proc. Appl. Math. Mech. **10**, 681 (2010).

[29] A. Parisi and R. C. Ball, Phys. Rev. B **72**, 054101 (2005).

[30] B. Kilic and E. Madenci, Int. J. Fract. **156**, 165 (2009).

[31] L. I. Slepyan, Dokl. Akad. Nauk SSSR **258**, 561 (1981) [Sov. Phys. Dokl. **26**, 538 (1981)].

[32] Sh. A. Kulamekhtova, V. A. Saraikin, and L. I. Slepyan, Izv. Akad. Nauk SSSR Mekh. Tverd. Tela **19**, 112 (1984) [Mech. Solids **19**, 102 (1984)].

[33] M. Marder and X. Liu, Phys. Rev. Lett. **71**, 2417 (1993).

[34] M. Marder and S. Gross, J. Mech. Phys. Solids **43**, 1 (1995).

[35] D. A. Kessler and H. Levine, Phys. Rev. E **59**, 5154 (1999).

[36] D. A. Kessler and H. Levine, Phys. Rev. E **60**, 7569 (1999).

[37] D. A. Kessler, Phys. Rev. E **61**, 2348 (2000).

[38] D. A. Kessler and H. Levine, Phys. Rev. E **63**, 016118 (2000).

[39] L. Pechenik, H. Levine, and D. A. Kessler, J. Mech. Phys. Solids **50**, 583 (2002).

[40] S. I. Heizler, D. A. Kessler, and H. Levine, Phys. Rev. E **66**, 016126 (2002).

[41] S. I. Heizler and D. A. Kessler, Cont. Mech. Thermodyn. **22**, 505 (2010).

[42] M. Marder and J. Fineberg, Phys. Today **49**(9), 24 (1996).

[43] S. J. Zhou, D. M. Beazley, P. S. Lomdahl, and B. L. Holian, Phys. Rev. Lett. **78**, 479 (1997).

[44] P. Gumbsch, S. J. Zhou, and B. L. Holian, Phys. Rev. B **55**, 3445 (1997).

[45] D. Holland and M. Marder, Phys. Rev. Lett. **80**, 746 (1998).

[46] H. Gao, F. F. Abraham, and M. J. Buehler, Nature (London) **426**, 141 (2003).

[47] M. J. Buehler and H. Gao, Nature (London) **439**, 04408 (2006).

[48] I. Procaccia, Eur. Phys. J. Spec. Top. **178**, 81 (2009).

[49] M. L. Falk and J. S. Langer, Phys. Rev. E **57**, 7192 (1998).

[50] M. L. Falk, Phys. Rev. B **60**, 7062 (1999).

[51] T. Y. Hirsh and D. A. Kessler, arXiv:cond-mat/0409607.

[52] O. Dauchot, S. Karmakar, I. Procaccia, and J. Zylberg, Phys. Rev. E **84**, 046105 (2011).

[53] S. I. Heizler, D. A. Kessler, and H. Levine, Phys. Rev. E **84**, 026102 (2011).

[54] W. H. Zachariasen, J. Am. Chem. Soc. **54**, 3841 (1932).

[55] F. Wooten, K. Winer, and D. Weaire, Phys. Rev. Lett. **54**, 1392 (1985).

[56] J. Astrom and J. Timonen, Phys. Rev. B **54**, R9585 (1996).

[57] J. Astrom, M. Alava, and J. Timonen, Phys. Rev. E **57**, R1259 (1998).

[58] P. Heino and K. Kaski, Phys. Rev. B **54**, 6150 (1996).

[59] P. Heino and K. Kaski, Phys. Rev. E **56**, 4364 (1997).

[60] P. Heino and K. Kaski, Int. J. Mod. Phys. C **8**, 383 (1997).

[61] D. A. Kessler and H. Levine (unpublished).

[62] A. Livne, E. Bouchbinder, and J. Fineberg, Phys. Rev. Lett. **101**, 264301 (2008).

[63] E. Bouchbinder, A. Livne, and J. Fineberg, Phys. Rev. Lett. **101**, 264302 (2008).

[64] G. N. Hassold and D. J. Srolovitz, Phys. Rev. B **39**, 9273 (1989).